

Study of a new-type of steel buckling-restrained brace

Jiang Tao^{1, 2†}, Dai Junwu^{1, 2‡}, Yang Yongqiang^{1, 2§}, Liu Yongbin^{1, 2†} and Bai Wen^{1, 2*}

1. Institute of Engineering Mechanics, China Earthquake Administration, Harbin 150080, China

2. Key Laboratory of Earthquake Engineering and Engineering Vibration of China Earthquake Administration, Harbin 150080, China

Abstract: The rectangle core plate of all-steel buckling-restrained braces (BRBs) usually exhibit obvious local buckling, due to the lack of longitudinal restraint from the encasing tube. To eliminate the undesirable effects, a novel steel BRB is proposed. In this new-type steel BRB, two T-shaped steels are adopted as the minor restraint elements to restrain the core plate instead of infilled concrete or mortar. Meanwhile, the ingot-iron material with low yielding strength and high elongation is applied to the steel core to study the mechanical properties of steel BRBs. To validate the theoretical requirements for the width-to-thickness ratio of the steel core and the thickness of angle steel, quasi-static tests of eight specimens were conducted. The tests focused on the energy dissipation capacity and failure modes of the proposed steel BRBs. Nonlinear finite element analysis was also carried out to validate the experimental results. Both the aforementioned results imply that appropriately designed steel BRBs can meet the performance requirements for BRB components.

Keywords: steel BRB; T-shaped steel; Ingot-iron; energy dissipation capacity; failure modes; nonlinear finite element analysis

1 Introduction

A typical buckling-restrained brace (BRB) is composed of a ductile steel core, which is designed to yield in both tension and compression. To preclude global buckling in compression, the steel core is usually wrapped with a steel casing, which is subsequently filled with mortar or concrete. Before casting mortar into the casing, an unbounded material or a very small air gap between the steel core and mortar is provided to minimize, or eliminate if possible, the transfer of axial force generated by the steel core to mortar and the steel casing. Considering the Poisson's effect, this small gap between the steel core and mortar is also needed to allow for the free expansion of the steel core. A variety of BRBs with different materials and dimensions have been proposed to date and a brief review of selected studies is present below.

Wakabayashi *et al.* (1973) first presented five specimens, in which the rectangle steel plate was embedded in the concrete slab. The experimental results revealed that these BRBs could demonstrate stable hysteretic behavior only if the critical buckling strength of the concrete slab was higher than that of the inner core. Kimura *et al.* (1976) subsequently developed a typical type of BRBs, where square steel pipe was adopted as the external restraint mechanism and the mortar was filled between the pipe and the steel core. Compared with conventional steel braces, the new devices exhibited great improvement on the overall buckling performance. However, in the low-cycle fatigue tests, the infilled mortar cracked and obvious local buckling on the steel core was observed.

In the early stages of BRBs development, mortar or concrete was usually filled between the external casing and the steel core to form the assistant restraint mechanism. However, this conventional BRB usually brought about not only transportation problems due to the bulkiness of concrete or mortar, but also inconvenience in field installation. Given that, all-steel BRBs, composed entirely with steel, were gradually developed. All-steel BRBs, taking full use of the steel material properties, significantly reduce manufacturing time and costs. In addition, compared with conventional BRBs, the component quality of all-steel BRB can be easily guaranteed.

Tsai *et al.* (2009) developed a new device called the multi-curve buckling restrained brace (MC-BRB), consisting of a core plate with multiple neck portions

Correspondence to: Dai Junwu, Institute of Engineering Mechanics, China Earthquake Administration, 29 Xuefu Road, Harbin 150080, China
Tel: +86-451-86652883
E-mail: junwudai@126.com

[†]PhD Candidate; [‡]Professor; [§]Associate Professor; ^{*}Assistant Professor

Supported by: Basic Research Foundation of Institute of Engineering Mechanics, CEA under Grant No. 2017A01, and the Earthquake Scientific Research Funds Program under Grant No. 201508023

Received September 21, 2018; **Accepted** May 5, 2019

assembled to form multiple energy dissipation segments. In order to investigate the behavior and seismic mitigation capability of this new device, component tests and a series of system tests were carried out at the NCEE. The experimental results demonstrated that the MC-BRB behaved in a stable mechanical manner under cyclic loading and could provide good protection to structures during earthquakes. Li *et al.* (2013) proposed H-shaped steel BRBs, assembled by two U-shaped steels, two steel plates and high-strength frictional bolts. The H-shaped steel BRBs exhibited stable hysteresis response with a large energy dissipation capacity. Kuwahara *et al.* (1993) developed a new form of BRBs, composed of a double-circular steel tube. The tests showed that BRB maximum ductility demand could be as high as 11. Sasaki *et al.* (2008) subsequently analyzed the effects of the internal and external steel pipe clearance and the ratio of diameter to thickness of such BRBs. It implied that the smaller the gap between the inner and outer steel pipe, the better the ductility. On the basis of previous research, Takeita *et al.* (2005) proposed a triple-tube combined BRBs, in which an additional steel pipe was added inside the steel pipe to make it sandwiched to preclude the local buckling.

Given that the radial range of steel pipe BRB was too narrow, Fukuda *et al.* (2004) attempted to replace the inner steel pipe with cross-section steel plate, and adopted angle steel as the external constraint element. However, when the component length was large, the configurations of these BRBs made it difficult to satisfy the overall stability demands.

In order to address the aforementioned problems, Ma *et al.* (2010) developed a type of BRB in which a cruciform steel core was restrained by a steel tube. This BRB exhibited high ductility and efficient energy dissipation. In addition, the experimental results also revealed that welding deformation and residual stress were critical to the mechanical properties of this BRB. Meanwhile, Koetaka *et al.* (2000) and Newell *et al.* (2006) also found that steel welding led to a significant reduction in fatigue performance for steel BRBs. To eliminate the welding effects, assembled steel BRBs were subsequently developed and gained popularity with the engineers. Eryasar and Topkaya (2010) designed a new form of steel BRBs and conducted low-cycle fatigue tests to study the hysteretic behavior, considering the number of bolts, length-to-thin ratio, width-thickness ratio and geometric defects on the steel core. The test results implied that the BRBs still behaved in a stable manner even when the axial strain of the steel core reached 2% or more. Jiang (2014) proposed a new type of BRB and developed the stiffness reduction factor for the external restrained casing. Based on the unique configurations, a set of design guidelines with regard to the double-tube steel BRB was put forward. Among these available BRBs, the advanced material technology applied to conventional BRBs has gradually gained popularity with scholars. Dusicka and Wiley (2008) developed a new type of BRBs, in which the aluminum alloy plate was

designed as the steel core and the glass fiber polymer was wrapped to serve as the restraint members. Miller *et al.* (2012) adopted N-T memory alloy as the steel core of BRBs, which could effectively reduce the earthquake damage on the structure. Deng *et al.* (2015) adopted four GFRP tubes as the constraint elements and wrapped them with GFRP to form relatively effective constraints. The BRBs exhibited stable hysteresis performance prior to the fracture on the steel core. During the tests, the GFRP tubes and cloths were seriously damaged due to the action of the steel core. To preclude the failure modes described above, the reinforcement guidelines were subsequently proposed.

In addition to the foregoing experimental research, many numerical simulations have been performed on isolated BRBs and BRB subassemblies in recent years (e.g., Fahnstock *et al.* (2003), López-Almansa *et al.* (2012), and Hoveidae and Rafezy (2015)). Although the research mentioned above has been conducted, there is still a long way to go before applying the steel BRBs in engineering practice since the configurations and fabrication are usually complicated. Moreover, local buckling behavior of the steel BRBs (e.g., local bulging of the constraint elements, undesirable local buckling occurred on the steel core along both the strong and weak axis, and obvious multi-wave buckling of the core plate and etc.) is still a challenge to engineers.

2 Research objectives

Note that Li *et al.* (2006) developed seven steel BRB specimens, in which a rectangle steel plate was adopted as the steel core while the steel tube was designed as the constraint element. Two typical failure modes were observed during the substructure pseudo-dynamic tests: the first occurred at the end of the steel tube at the loading displacement of 5.36 mm (as shown in Fig. 1(a)); the other presented as the steel tube became wavy (as shown in Fig. 1(b)), indirectly implying the high-order buckling mode of the steel core. To preclude these premature failure modes, a novel all-steel BRB is proposed in this study. A comparison between the two different all-steel BRB configurations is shown in Fig. 2.

In this new device, the T-shaped steel is welded to the angle steel to provide lateral constraint on the core plate. Compared with infilled mortar and concrete, the T-shape steel possesses sufficient margin to resist the lateral thrust generated by the inner core in compression. In addition, the core plate adopts two kinds of materials: one is steel Grade Q235B, and the other is ingot iron. The material of ingot iron is a kind of steel, in which the content of iron ranges from 99.50% to 99.90% while the content of carbon is restrained within 0.04%. The specimen with Q235 is intended to validate the rationality of this new BRB, while the steel core with ingot iron is designed to explore whether this new material with low yield strength and high deformation

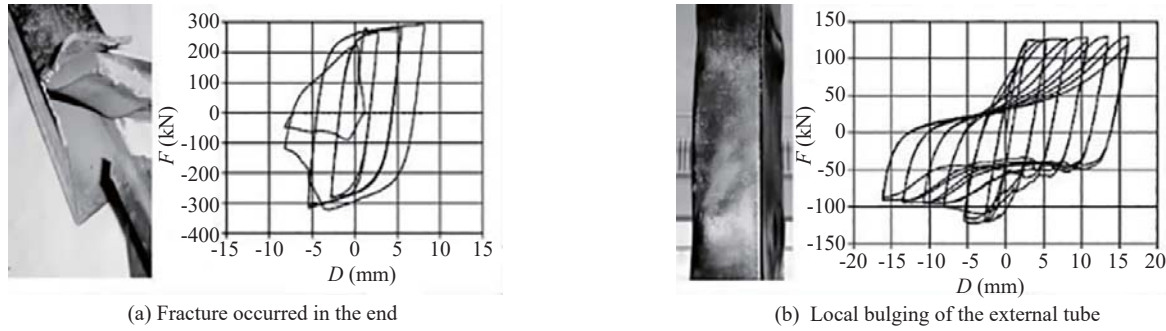


Fig. 1 Two typical failure modes observed during the test

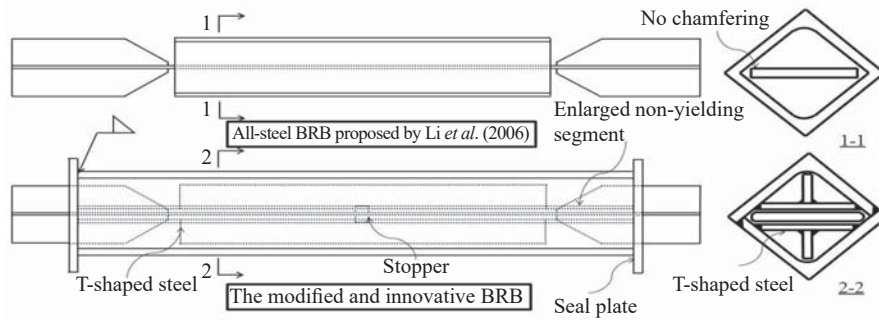


Fig. 2 Specimen setup

capacity is a better choice. Moreover, to preclude the rupture at the end of the restrained elements, the seal plates are welded to both ends of the angle steel. Based on the available design guidelines on steel BRBs, eight specimens were configured in detail. Quasi-static tests were also conducted on the new BRBs to test the mechanical properties, hysteretic behavior and fatigue performance, considering different width-to-thickness ratios of inner core, different materials of inner core, and different thickness of corner steel. Finally, the finite element analysis was carried out to validate the experiment results.

3 Design requirements for steel BRBs

3.1 Overall flexural buckling

Previous studies reveal that BRBs usually suffer from first-order flexural buckling of the steel core and the external restraint member, which is defined as overall flexural buckling. Mochizuki and Murata (1979) found that the bearing capacity of steel BRBs in global flexural buckling can be expressed as follows:

$$P_e = \frac{\pi^2 E_r I_r}{L_t^2} \quad (1)$$

where $E_r I_r$ is the bending stiffness of the restraint member;

and L_t is the total length of the BRB. According to the current Chinese code, Chinese Technical Specification for Steel Structure of Tall Buildings (JGJ 99-2015, 2015), P_e should satisfy the following criterion:

$$\zeta = \frac{P_e}{P_u} \geq 1 \quad (2)$$

where ζ denotes the constraint ratio, namely the ratio of the bearing capacity in global flexural buckling P_e to the ultimate bearing capacity P_u of the steel core. The ultimate bearing capacity P_u can be calculated as follows:

$$P_u = \beta \omega P_y \quad (3)$$

$$P_y = \eta_y f_{ay} A_c \quad (4)$$

where P_y is the measured yielding strength of BRB, which is determined from the coupon test; η_y is the overstrength factor of the material; f_{ay} is the standard yielding strength of the steel core, and A_c denotes the net area of the steel core; β is the compression strength adjustment factor, determined by the ratio of the compressive bearing capacity to the tensile bearing capacity; and ω denotes the strain hardening factor. The values of β and ω are conservatively taken as 1.3 and 1.5 based on the available experimental data of Watanabe *et al.* (1998), Black *et al.* (2004). Equation (2) can be

expressed as follows:

$$\zeta = \frac{P_e}{P_u} \geq 1.95 \quad (5)$$

3.2 Local stability of steel core

Previous research implies that the width-to-thickness ratio of the core plate has an important impact on the local stability. If the width-to-thickness ratio is too small, the thrust force generated by the steel core may lead to local bulging of the constraint elements. In view of this, it is necessary to determine rational values for the width-to-thickness ratio of the steel core. In this new device, the core plate is nearly wrapped by the T-shaped steel. According to the beam on elastic foundation assumption (Wang *et al.*, 2007), the T-shaped steel can be equivalent to an elastic foundation, and the distributed load $q(x)$ provided by the T-shaped steel to the steel core can be expressed as:

$$q(x) = \lambda y(x) \quad (6)$$

$$\lambda = E_0(1-\nu)/(1+\nu)(1-2\nu) \quad (7)$$

where λ denotes the spring constant or the elastic constraint stiffness of the T-shaped steel; ν is Poisson's ratio; E_0 is the elastic modulus for the T-shaped steel; and $y(x)$ denotes the deflection of the steel core. The balanced differential equation for the steel core can be derived as follows:

$$E_c I_c \frac{d^4 y}{dx^4} + P \frac{d^2 y}{dx^2} + \lambda y = 0 \quad (8)$$

To solve this differential equation, the first-mode buckling load $P_{cr,1}$ of the steel core can be obtained:

$$P_{cr,1} = 2\sqrt{\lambda E_c I_c} \quad (9)$$

where E_c is the elastic modulus for the steel core; and I_c denotes the inertial moment of the steel core.

To preclude local buckling prior to yielding, the limit of the width to thickness ratio for the steel core can be expressed as follows:

$$\frac{b_c}{t_c} \leq \frac{E_0 E_c (1-\nu)}{3 f_y^2 (1+\nu)(1-2\nu)} \quad (10)$$

where b_c is the width for the steel core; t_c denotes the thickness for the steel core; and f_y is yielding strength for the steel core.

3.3 Clearance conserved between steel core and external restraint members

Given that the steel core is usually regarded as a long and thin rod in the longitudinal direction, it can be simplified as a tension and compression rod. Under axial force, it could generate a high-order elastoplastic buckling mode, and the thrust force would be exerted to the external restraint elements. Ma (2010) revealed that the ratio of the gap between the steel core and external angle steel to the width of the steel core is critical to the thickness design of the external angle steel. Therefore, to accommodate lateral expansion of the steel core due to Poisson's effect in compression, Ma (2010) found that the gap δ between the steel core and the T-shape steel should satisfy the following equation:

$$2\delta \geq 0.5 b_c \varepsilon_{\max} \quad (11)$$

where ε_{\max} is the maximum axial strain. Meanwhile, the ratio of the gap between the steel core and the T-shape steel to the width of the steel core μ can be governed as follows:

$$\mu = \frac{\delta}{b_c} \geq \frac{\varepsilon_{\max}}{4} \quad (12)$$

In general, the axial deformation of BRBs should be up to 3%, which means μ should be greater than 0.75%.

3.4 Bending strength requirements for restraint members

Assuming that the initial deflection of the steel core follows a sinusoidal distribution, the balanced differential equation for BRBs can be derived as follows:

$$E_r I_r \frac{d^2 v}{dx^2} + P_u (y + y_0) = 0 \quad (13)$$

$$y_0 = a \sin \frac{\pi x}{L_t} \quad (14)$$

where y_0 means the initial deflection of the steel core; and a denotes the initial mid-span deflection of the steel core. According to the current Chinese code, Chinese Technical Specification for Steel Structure (GB 50017-2017, 2017), the value of a is generally taken to be $0.002 L_t$.

The deformation in the mid-span of the BRB can be calculated as follows:

$$y + y_0 = \frac{a}{1 - \frac{P_e}{P_u}} \sin \frac{\pi x}{L_t} \quad (15)$$

The maximum bending moment in the mid-span of the external restraint members M can be calculated by

the following equation:

$$M = P_u (y + y_0)_{\max} = \frac{P_u P_e a}{P_e - P_u} \quad (16)$$

The restraint members should provide sufficient flexural capacity, which means the bending strength of the restraint members M_u should be greater than M . M_u can be calculated as follows:

$$M_u = W_p f_s \quad (17)$$

where W_p denotes the effective plastic section modulus of the constraint members, which can be calculated with the aid of AutoCAD; and f_s denotes the yielding strength of the external restraint members.

3.5 Bearing capacity requirements for unrestrained non-yielding segment

This segment is usually regarded as an extension of the restrained non-yielding segment of the steel core. Projecting from the casing for the connection to the frame, this segment is generally designed as the cross section. However, this segment often suffers from torsional buckling due to a lack of effective restraint from the external casing.

Black *et al.* (2002) found that the elastic torsional critical buckling stress σ_{cr} of the cross section can be calculated by the following equation:

$$\sigma_{cr} = \frac{\pi^2 E_c}{12(1-\nu^2)} \frac{t_j^2}{b_j^2} \left[\frac{b_j^2}{l_j^2} + \frac{6(1-\nu)}{\pi^2} \right] \quad (18)$$

where E_c denotes the elastic modulus of the steel core; l_j is the length of the unrestrained nonyielding segment; b_j is the width of the unrestrained nonyielding segment; and t_j is the thickness of the unrestrained nonyielding segment. For long plates where $l_j \gg b_j$, the term b_j^2 / l_j^2 vanishes and Eq. (18) reduces to

$$\sigma_{cr} = \frac{E_c}{2(1+\nu)} \frac{t_j^2}{b_j^2} \quad (19)$$

In order to preclude the torsional failure of the unrestrained nonyielding segment, the design value of the torsional buckling load for the cross section should usually be greater than the measured yield strength ($\sigma_{cr} \geq f_y$).

$$\frac{b_j}{t_j} \leq \sqrt{\frac{E_c}{2(1+\nu) f_y}} \quad (20)$$

In view of Eq. (20), it is recommended that the width-to-thickness ratio b_j/t_j of the unrestrained

nonyielding segment should not exceed 18.1. However, in the derivation of the aforementioned formulas, the three flanges of the cross section are assumed to be fixed while the remaining one is free. Wu (2008) found that the constraints on the nonyielding segment from the core plate and gusset plate were slightly overestimated. Based on the FEM analysis, the boundary conditions of the nonyielding segment are assumed to be hinged, and the width-to-thickness ratio is conservatively taken as no more than 13.

4 Test program

4.1 Specimens

Eight steel BRB specimens are designed, and the configurations are shown in Fig. 3, in which L_t denotes the total length of the BRB specimens; L_{tl} and L_{ry} are the lengths of the unrestrained segment and restrained yielding segment, respectively; b_{c1} and b_{c2} are the widths of the rectangular cross section of the steel core and stiffener; t_{c1} and t_{c2} are the thickness of rectangular cross section of the steel core and stiffener; and w and d are the length and thickness of the cross section of the external angle steel, respectively. L_{c1} and L_{c2} are the lengths of the notch and the stiffener for the T-shaped steel, respectively; b_{l2} and b_{l3} are the widths of the rectangular cross section of the stiffener and the notch, respectively; and t_{l1} and t_{l2} are the thickness of the rectangular cross section and the stiffener for the T-shaped steel. Considering the steel core would shrink in compression, the reserved gap is designed at the end of the notch to preclude the conflict between the steel core and T-shaped steel (see Fig. 3(d)). T-shaped steel is connected to the angle steel through spot welding (see Section 1-1, 2-2 in Fig. 3(d)).

The geometric dimensions of the BRB specimens are illustrated in Table 1. For convenience, these BRBs are labelled as “Q (or I) – 1”, in which ‘Q’ and ‘I’ refer to the material applied to the steel core. Two types of angle steels are adopted as the restraint elements: “Q-1 to 2, I-1 to 2” and “Q-3 to 4, I-3 to 4” refer to the angle steel with $d = 6$ mm and $d = 8$ mm, respectively; Two types of rectangular plates are adopted as the steel core: “Q-1, Q-3, I-1, I-3” and “Q-2, Q-4, I-2, I-4” refer to the core plate with $b_c/t_c = 8.0$ and $b_c/t_c = 10.0$, respectively.

The steel of Grade Q235-B and ingot-iron are adopted as the material of the steel core, while the steel of Grade Q345 is applied to the angle steel, T-shaped steel and stiffeners. The tensile tests of the steel were conducted to obtain the experimental stress-strain curves and the mechanical parameters. The nominal stress-strain curves in uniaxial tension (i.e., force divided by initial area of the cross section versus displacement divided by initial length) for the steel core and the angle iron are shown in Fig. 4. In addition, the mechanical parameters for the steel are shown in Table 2, in which f_y denotes the measured value of the yielding strength, f_u is the ultimate tensile strength, and E_s is the elastic modulus for the steel.

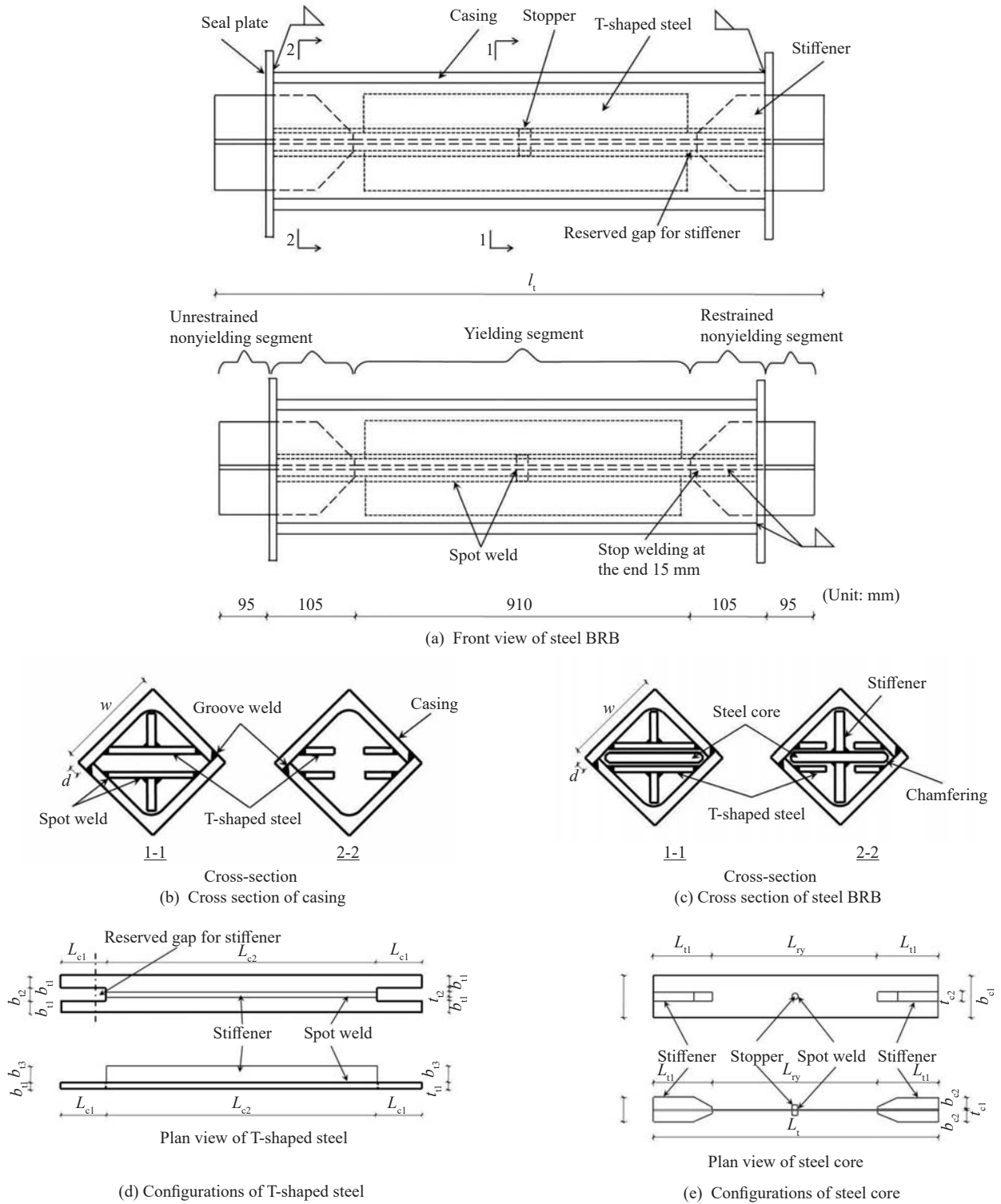


Fig. 3 Specimen setup

As shown in Fig. 4, there is no visible yield plateau for ingot-iron, and the inelastic deformation is outstanding. On the basis of the coupon tests, some key specimen parameters, such as P_y , ζ , M and M_u , can be determined by the foregoing equations. Based on the specimens parameters illustrated in Table 3, eight BRB specimens can be divided into the following three categories:

(1) Width-to-thickness ratio b/t for the steel core

As described above, the width-to-thickness ratio is critical to local buckling of the steel core. Ma (2010) found that the width-to-thickness ratio for the rectangular core plate should be set around 8. In view of this, two groups of specimens with $b/t = 8.0$ (Q-1, Q-3, I-1, I-3) and $b/t = 10.0$ (Q-2, Q-4, I-2, I-4) were configured,

respectively, to investigate the local buckling issues.

(2) Thickness d for the angle steel

The thickness of the angle steel has a great impact on the bending strength of the casing. Ma (2010) found that the thickness d is vital to the local buckling of the external restraint elements, and the casing without

T-shaped steel should be at least 8 mm. Given that, two groups of specimens with thickness $d = 6$ mm (Q-1 to 2, I-1 to 2) and $d = 8$ mm (Q-3 to 4, I-3 to 4) are designed, respectively, to investigate the local buckling issues.

(3) Material applied to the steel core

Two types of material with steel grade of Q235B and ingot-iron are adopted as the steel core to explore whether ingot-iron with low yield strength and high ductility is a better choice for the steel core.

Figure 5 shows the fabrication process of the T-shaped steel and steel core used for the specimens. T-shaped steel is composed of a stiffener and a rectangular steel plate (see Fig. 5(a)). As shown in Fig. 5(a), the stiffener is attached to the steel plate by spot welding. Considering the contact between the steel core and the casing, the edges of the steel core plate are chamfered (see Fig. 5(b)). To prevent the axial rigid body movement of the restraining element, the stopper is placed in the mid-span of the steel core by spot welding (see Fig. 5(c)). Considering the flexural strength requirements, the end portions of the steel core are enlarged through stiffeners to form a cruciform section (see Fig. 5(d)). To prevent excessive stress concentration in the vicinity of stiffeners, the weld joint is usually stopped at a distance of 15 mm from the end of the stiffener. PVC plastic is used as the unbounded agent to eliminate the transfer of shear force between the restrained segment and casing

Table 1 Specimen sizes (unit: mm)

Specimens	Steel core	$b_{cl} \times t_{cl}$	$w \times d$	L_t
Q-1	Q235-B	80×10	75×6	1310
Q-2	Q235-B	80×8	75×6	1310
Q-3	Q235-B	80×10	80×8	1310
Q-4	Q235-B	80×8	80×8	1310
I-1	Ingot-Iron	80×10	75×6	1310
I-2	Ingot-Iron	80×8	75×6	1310
I-3	Ingot-Iron	80×10	80×8	1310
I-4	Ingot-Iron	80×8	80×8	1310

Table 2 Characteristics of steel

Steel	f_y (MPa)	f_u (MPa)	f_u/f_y	E_s (MPa)
Q235-B	281	461	1.63	2.03×10^5
Ingot-Iron	215	305	1.42	1.95×10^5
Casing	371	520	1.40	2.01×10^5

Table 3 Specimen parameters

Specimens	P_y (kN)	P_c (kN)	ζ	M_u (kN·m)	M (kN·m)	b_c/t_c	δ/t_c (%)
Q-1	225	6275	28	17.60	0.611	8.0	1.00
Q-2	180	6275	35	17.60	0.485	10.0	1.25
Q-3	225	9504	42	24.99	0.603	8.0	1.00
Q-4	180	9504	53	24.99	0.480	10.0	1.25
I-1	172	6275	37	17.60	0.463	8.0	1.00
I-2	138	6275	46	17.60	0.369	10.0	1.25
I-3	172	9504	55	24.99	0.458	8.0	1.00
I-4	138	9504	69	24.99	0.366	10.0	1.25

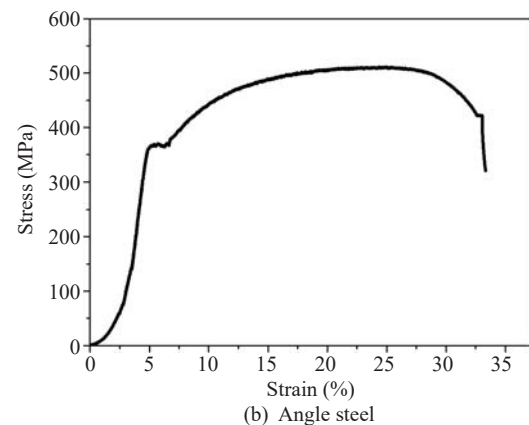
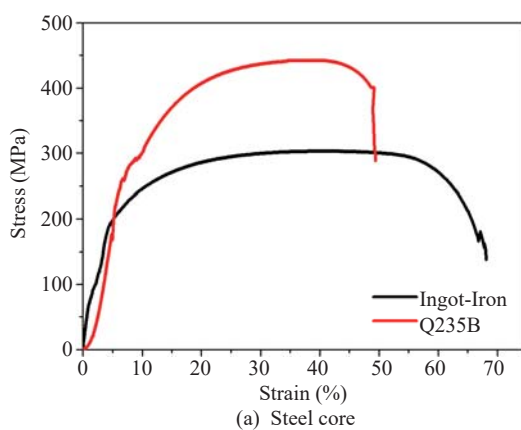


Fig. 4 Stress-strain curves of steel

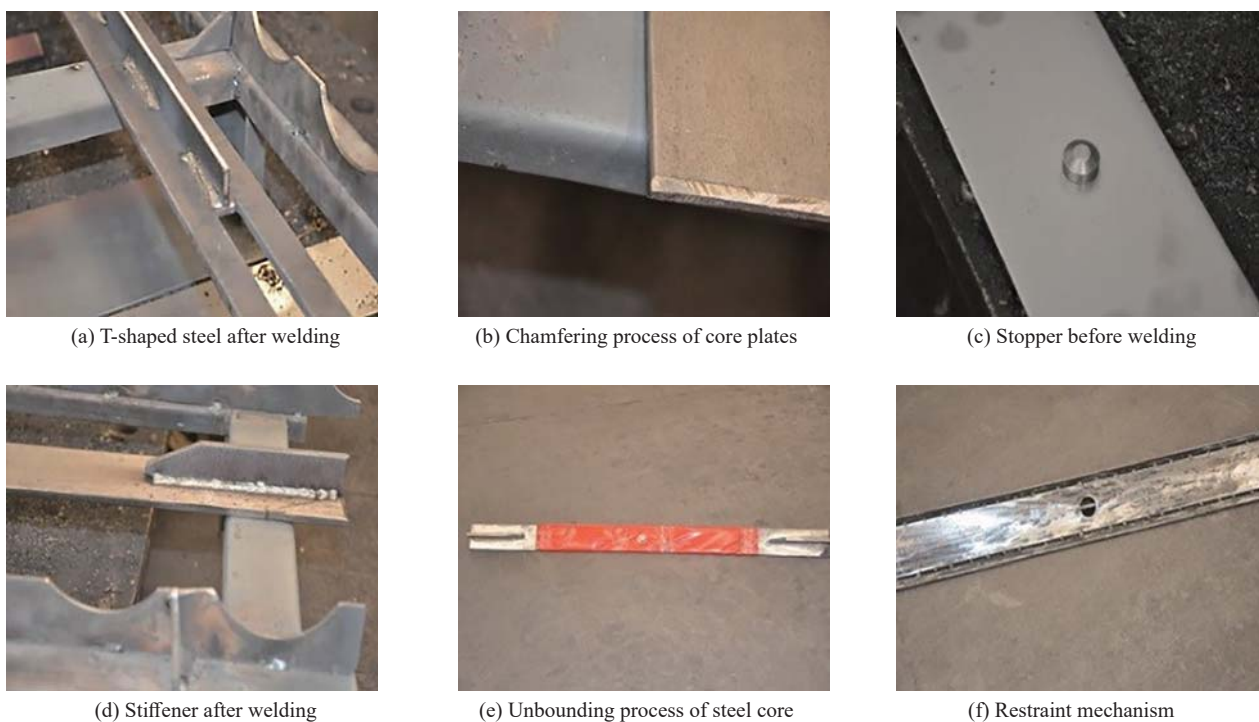


Fig. 5 Fabrication process of T-shaped steel and steel core

(see Fig. 5(e)). As shown in Fig. 5(f), T-shaped steel is welded to the angle steel.

Figures 6(a) and 6(b) present the assembly process of the casing, in which the angle steel was connected by groove welding. In addition, the seal plates were welded to both ends of the angle steel to make the external restraint members a whole. The core plate was welded onto a thick steel plate for connection to the loading apparatus (see Fig. 6(c)). To preclude the premature rupture at the end of the steel core, triangle reinforced plates were added for strengthening (see Fig. 6(c)).

4.2 Test setup

The self-balancing loading apparatus is shown in Fig. 7 and Fig. 8(a). This device, composed of a 1000 kN dynamic actuator, the rail system, can make the slider freely slide to ensure the axial loading. In order to accurately obtain the axial displacement, two

LVDT sensors are symmetrically placed at both ends of the specimens (see Fig. 8(c)). Meanwhile, a draw-wire displacement sensor is placed between the two loading connection plates to measure the overall axial displacement (see Fig. 8(d)). The axial displacement of the restrained yielding segment is achieved by subtracting the values of two linearly variable displacement transducers (LVDTs). To monitor the out-of-plane displacement of the specimens in real-time, two dial indicators are symmetrically placed in the middle of the casing (see Fig. 8(b)).

The axial displacement of the specimen is controlled with displacement during the loading process. Moreover, a stepwise incremental quasi static cyclic test protocol is imposed on the specimens at axial strain amplitudes of $1/300$, $1/200$, $1/150$, $1/100$, and $1/66$ (with three times each except $1/150$), as shown in Fig. 9. Particularly, thirty constant amplitude cycles at the axial strain of 1% are designed to check the low-cycle fatigue performance

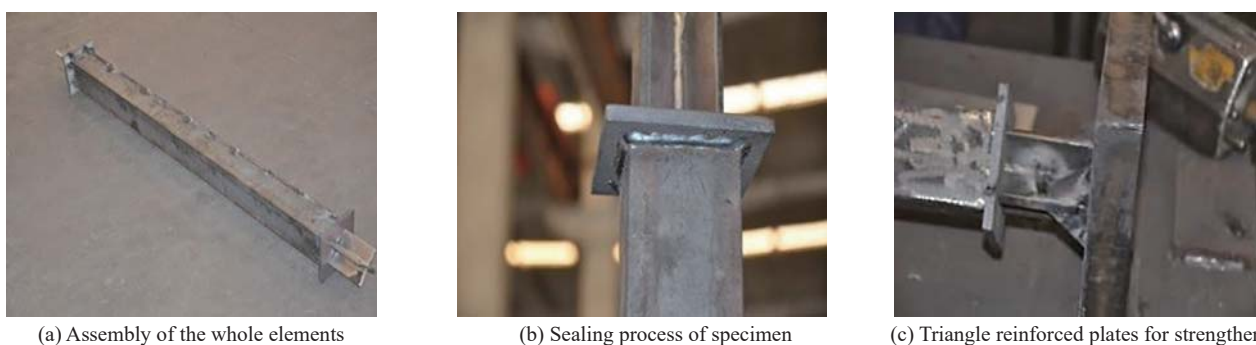


Fig. 6 Assembly process of specimens

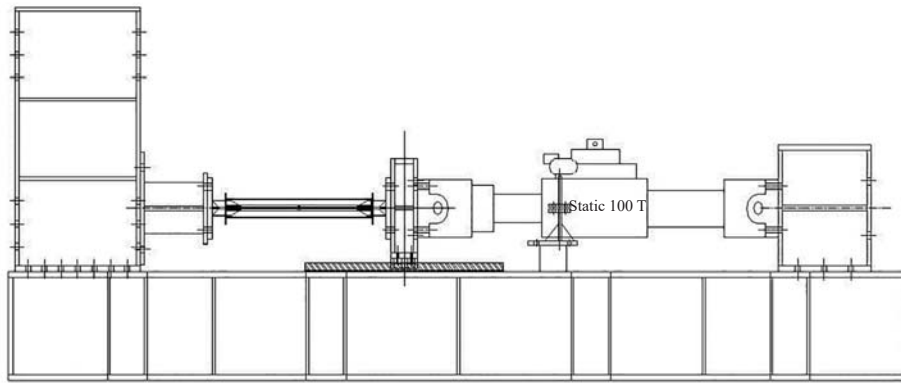
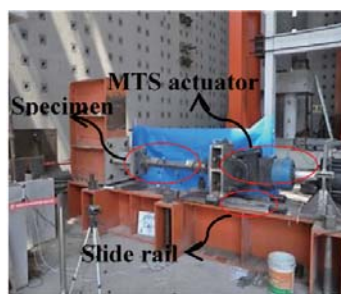


Fig. 7 MTS test devices



(a) Factual MTS test devices



(b) Dial indicator



(c) Draw-wire sensor



(d) LVDTs

Fig. 8 Test measurement devices

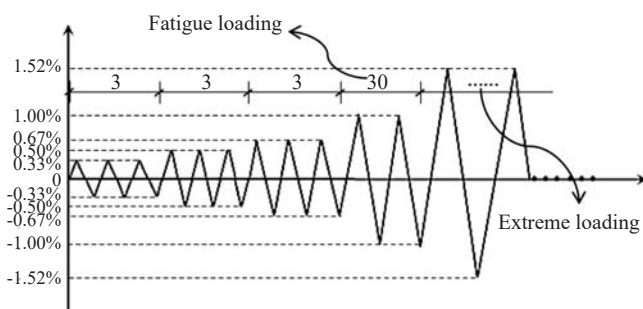


Fig. 9 Graphical expression of loading protocol

of the specimens. If the specimen withstands low-cycle fatigue tests, the loading magnitude would increase to $1/66$ until the specimen fails. In addition, all the loading steps start with compression and the loading rate is 0.8 mm/s .

4.3 Test phenomenon

This section presents the test phenomena and the

failure modes of the eight specimens. All eight specimens were found to be invalid due to the rupture of the steel core. During the loading process, the maximum values of the dial indicators were around 1.0 mm (less than $L_t/500 = 2.0 \text{ mm}$), which indicated that the overall buckling failure mode did not occur in the test. Figure 10 shows the typical failure modes of the core plates observed after the tests. It was found that fracture of the specimens with steel Grade of Q235B occurred in the vicinity of the stiffener ends (see Figs. 10(a)–10(d)), while for the specimens with ingot-iron, fracture occurred in the middle of the core plates (see Figs. 10(e)–10(h)).

In addition, Figs. 11(a)–11(h) show the global deformation of the core plates. The specimens with ingot-iron exhibited obvious multiple-wave buckling modes, while the specimens with steel Grade of Q235B displayed no obvious deformation.

As depicted in Fig. 12, no obvious damage was observed on T-shaped steel and angle steel after tests. The spot welding joints, connecting the angle steel and T-shaped steel, were found to be in working condition

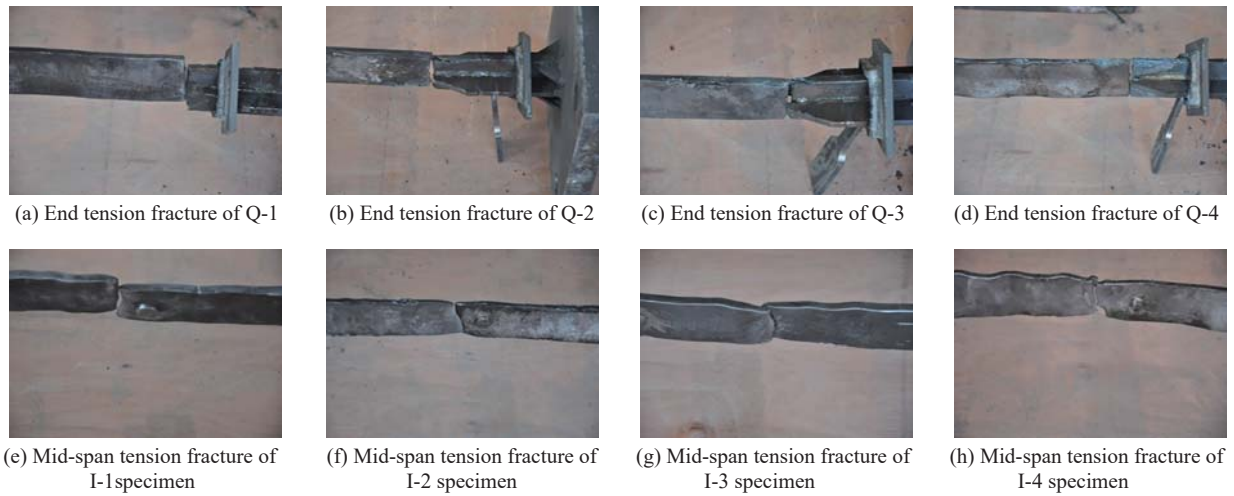


Fig. 10 Failure modes of specimens

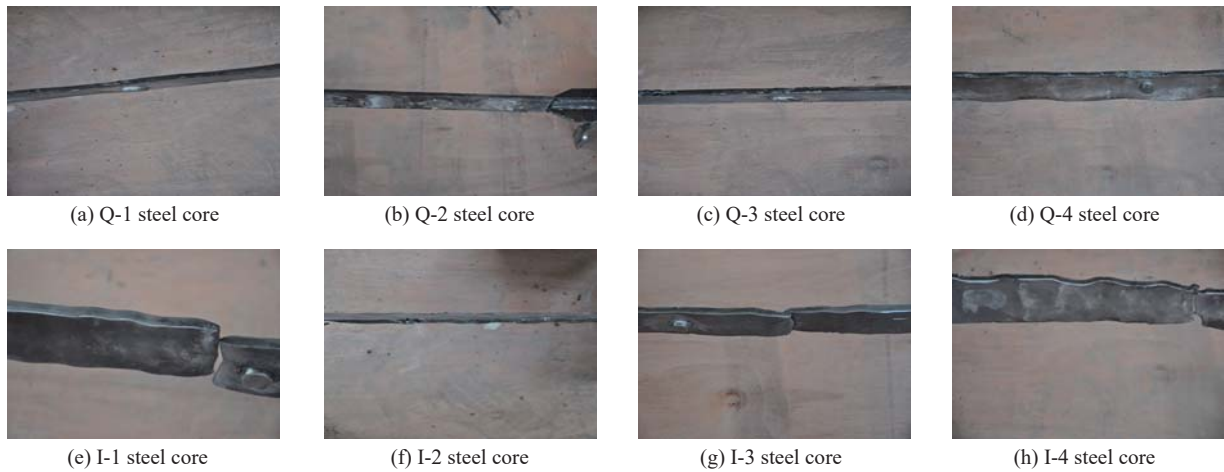


Fig. 11 Multiple-wave buckling modes of steel core



Fig. 12 Casing split after test

after the tests. Meanwhile, there was no obvious local bulging observed on the external constraint elements, which demonstrated that the T-shaped steel possessed sufficient margin to resist the lateral thrust generated by the inner core in compression.

4.4 Hysteretic behavior

Figures 13(a)–13(h) show the hysteretic loops of the eight specimens. All eight specimens exhibited stable

hysteretic behavior before the fatigue loading phase. The hysteretic loops of the Q-series specimens can be approximated as a spindle, while the specimens with ingot-iron appear to be a parallelogram.

Figures 14(a)–14(h) show the hysteretic loops of the eight specimens in low-cycle fatigue tests. All the specimens with steel Grade of Q235-B had failed due to the fracture of the steel core, where the specimen Q-1 cycled 15 times; Q-2 cycled 9 times; Q-3 cycled 10 times; and Q-4 cycled 24 times. However, all the

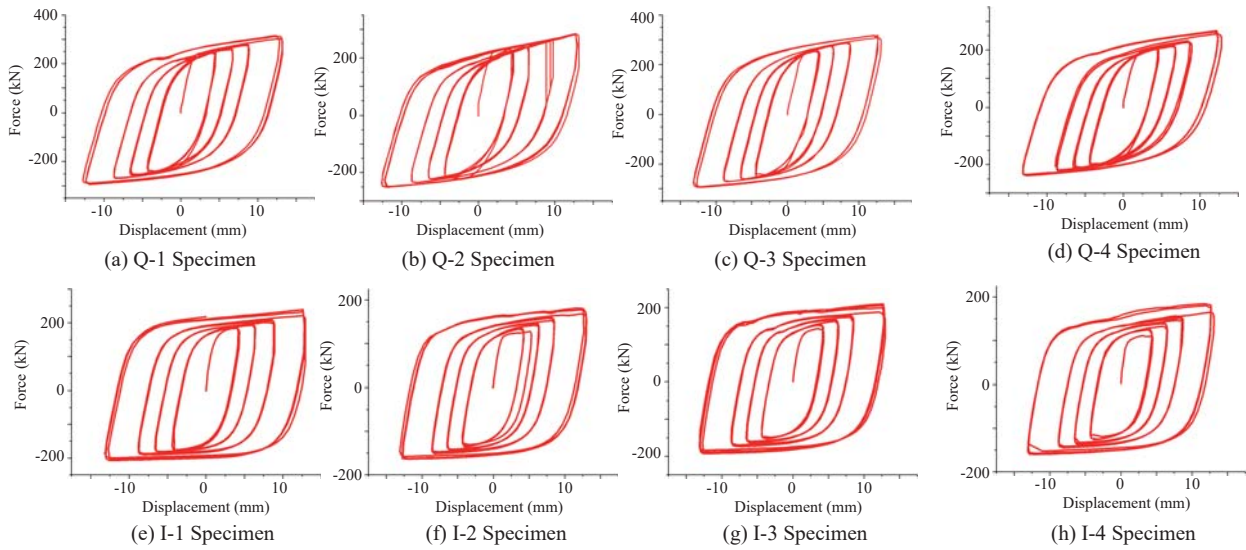


Fig. 13 Recorded hysteresis curves of steel BRBs

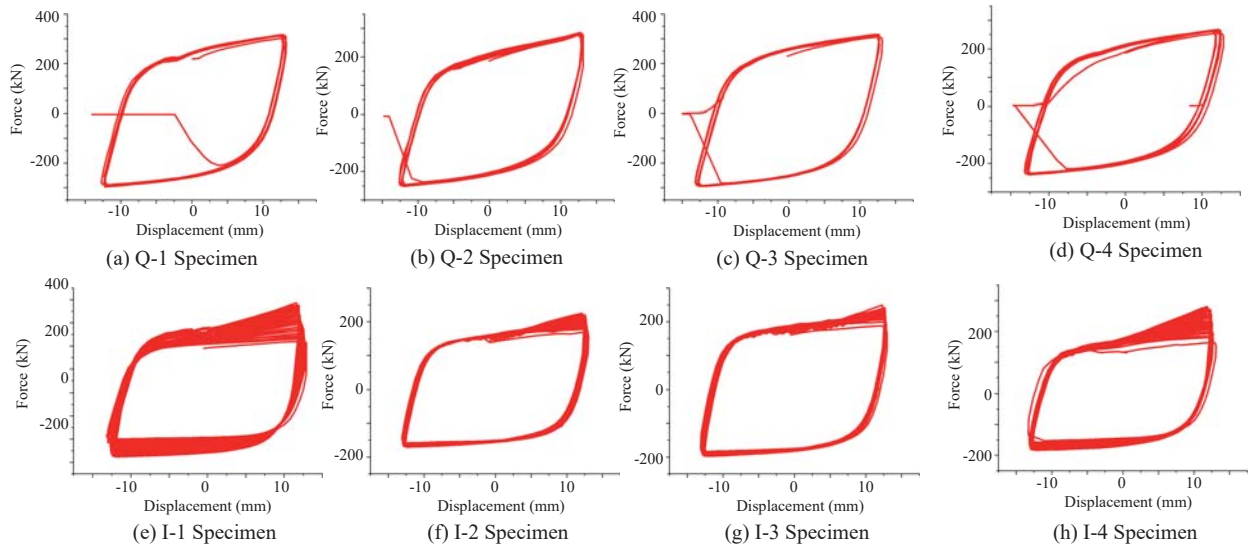


Fig. 14 Recorded hysteretic loops of specimens in fatigue loading phase

I-series specimens had withstood the 30 cycles of fatigue loading without any decline in bearing capacity, which and therefore exhibited excellent ductility. Furthermore, the hysteretic curves of the I-series specimens exhibited dramatic cyclic hardening in compression, which indicated the occurrence of high-order buckling modes on the steel core.

4.5 Performance assessment

(1) Compression strength adjustment factor, β :

Due to the transfer of axial force between the steel core and casing, the compression strength of BRB is usually higher than the tensile strength. This is a small unbalance, but nonetheless it must be taken into account from a capacity design point of view. Hence, compression strength adjustment factor β is introduced to assess the over-compression of BRB as

$$\beta = \frac{C_{\max}}{T_{\max}} \quad (21)$$

where C_{\max} and T_{\max} represent the maximum compression and tension forces of the specimens, respectively.

(2) Strain hardening adjustment factor, ω :

If the steel has suffered from subsequent yielding in compression and tension, the phenomenon of strain strengthening would arise, namely the stress would exceed the initial yield surface. Therefore, the strain hardening adjustment factor, ω , is applied to evaluate the ratio of the maximum tensile force to the measured yielding strength as:

$$\omega = \frac{T_{\max}}{P_y} \quad (22)$$

(3) Cumulative plastic ductility, CPD:

Ductility is one of the most important indexes, which intuitively reflects the seismic performance of BRBs. Given that, CPD is introduced to evaluate the cumulative plastic deformation, which is defined as the following expression:

$$CPD = \sum_i \left[2 \left(\left| \Delta_{\max}^i \right| + \left| \Delta_{\min}^i \right| \right) / \Delta_y - 4 \right] \quad (23)$$

where Δ_{\max}^i and Δ_{\min}^i are the maximum positive and negative plastic deformations of BRB in the i th loading cycle, respectively; Δ_y denotes the yielding displacement.

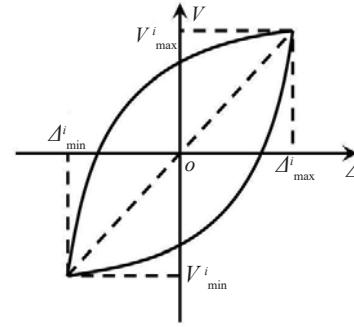
As listed in Table 4, the compression strength adjustment factor, β of Q-series specimens ranges from 1.07 to 1.23, which satisfies the upper limit of 1.3 specified in the AISC/SEAOC recommended provisions for buckling-restrained braced frames (2001). With regard to I-series specimens, the computed β factors range from 1.29 to 1.51. From the deformation of the steel core shown in Fig. 8, it is clear that the steel core with ingot-iron had experienced the high-order buckling mode. Therefore, the shear force (frictional force) would have a significant impact on the over-compression, and lead to an increase of the factor, β .

Similarly, the strain hardening adjustment factor, ω of Q-series specimens ranges from 1.14 to 1.27, while the ω of I-series specimens ranges from 1.57 to 2.00. As depicted in Fig. 10, I-series BRBs exhibit obvious strengthening and hardening in the fatigue loading phase, which is a typical characteristic for steel with low yielding strength.

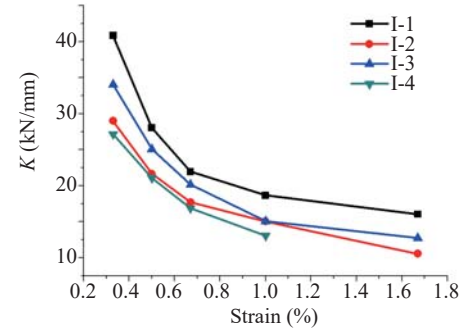
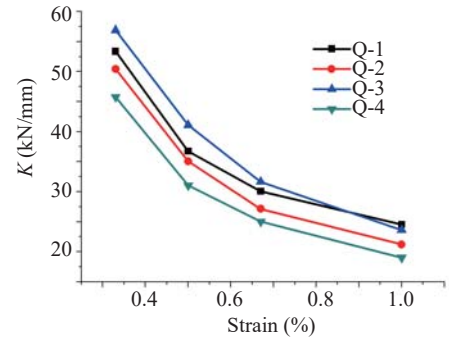
In view of the definition of CPD, there is no doubt that it would increase with the augment in the loading cycles. Meanwhile, all the Q-series specimens failed during the fatigue tests, while the I-series specimens were still in working condition. Therefore, as illustrated in Table 8, the CPD with I-series specimens is far better than that for the Q-series specimens.

(4) Equivalent secant stiffness, K :

During each loading cycle, the inclination between two extreme points in compression and tension is adopted as the equivalent secant stiffness of the specimen (see in Fig. 15(a)). The equivalent secant stiffness, K



(a) Definition of K_i



(b) Equivalent secant stiffness of specimens

Fig. 15 Equivalent secant stiffness

could intuitively reflect the overall stiffness variation of the specimens during tests, which is calculated by the following expression:

$$K_i = \frac{|V_{\max}^i| + |V_{\min}^i|}{|\Delta_{\max}^i| + |\Delta_{\min}^i|} \quad (24)$$

where K_i is the secant stiffness of the i th loading step; and V_{\max}^i and V_{\min}^i are the maximum positive and negative load of BRB in the i th loading step.

(5) Equivalent viscous damping coefficient, h_e :

The equivalent viscous damping coefficient denotes the ratio of the dissipated energy (the area of ABCD) to the absorbed energy (the area of OBE and OFD) of the equivalent elastic component that undergoes the same displacement (see in Fig. 16(a)). The equivalent viscous damping coefficient could demonstrate the change in energy consumption of the BRB during cyclic

Table 4 Assessments for specimens

Specimen	ω	β	Cycling number	CPD
Q-1	1.26	1.07	24	221.61
Q-2	1.14	1.23	18	191.83
Q-3	1.35	1.12	19	176.53
Q-4	1.27	1.21	33	335.52
I-1	2.00	1.36	42	665.07
I-2	1.57	1.29	42	583.92
I-3	1.73	1.43	42	698.46
I-4	1.81	1.51	43	573.94

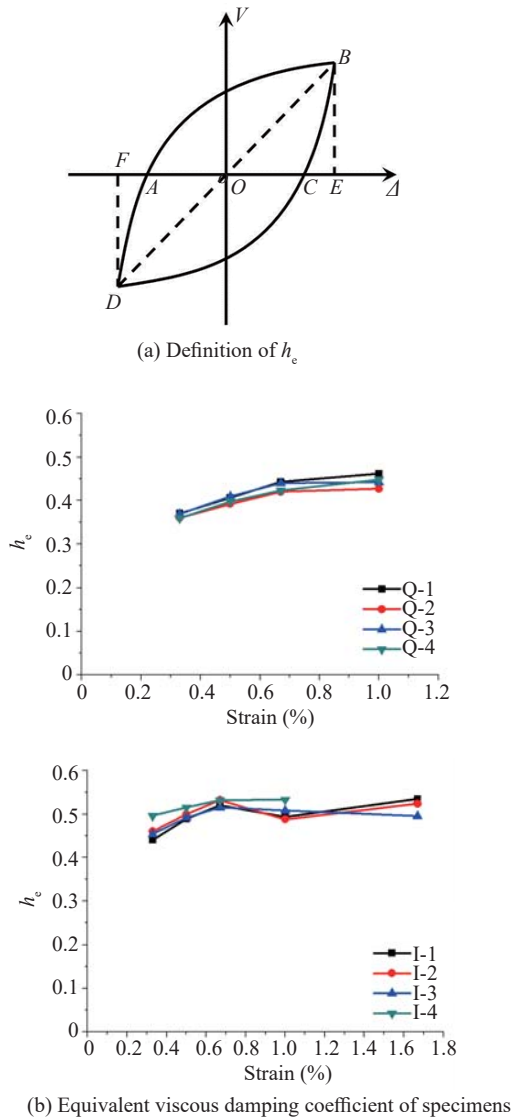


Fig. 16 Equivalent viscous damping coefficient

loading. The equivalent viscous damping coefficient, h_e is calculated by the following expression:

$$h_e = \frac{1}{2\pi} \frac{S_{ABCD}}{S_{OBE} + S_{OFD}} \quad (25)$$

As shown in Fig. 15(b), the equivalent secant stiffness decreases with the growth of the axial strain, which reflects the stiffness degradation of the steel core. Moreover, the width-to-thickness ratio of the steel plates that are equal to 8 (Q-1, Q-3, I-1 and I-3) and possess higher equivalent secant stiffness when compared with the width-to-thickness ratio equal to 10 (Q-2, Q-4, I-2 and I-4).

Figure 16(b) presents the relationship between the equivalent viscous damping coefficient and the axial strain. Compared with the steel core with steel grade of Q235B, the I-series specimens exhibit a more distinguished performance with regard to energy consumption.

5 BRB finite element analysis

5.1 Finite element model description

To analytically investigate the seismic performance of the BRB and contrast it to the experimental results, eight steel BRBs are modeled using the general purpose finite element analysis program Abaqus. As shown in Fig. 17, all the members of steel BRB are modeled using eight-node solid elements (C3D8R). Rigid links are used to model weld joints between the stiffener plate and the steel core. Tie constraints are adopted to simulate the connection between the T-shaped steel and casing. Furthermore, due to Poisson's effects of the steel core in compression, it is clear that the steel core would come into contact with the T-shaped steel and casing. To model this highly nonlinear behavior, the contact properties between the steel core and the restraint members are established to consider both normal and tangential behavior of the contact interface. The tangential behavior is simulated through the definition of the frictional coefficients on the contact interface. The "hard contact" is adopted to simulate the normal behavior, allowing the separation of the steel core and casing when the clearance between them is negative. In addition, the damping factor for contact control was set to be 1×10^{-4} to achieve a better convergence in the simulation process.

Meanwhile, to simplify the influence of the initial defects (with respect to the fabrication, welding, etc.) on the performance of steel BRB, the first-order buckling mode with a central amplitude of 1/1000 of the BRB length is taken as the initial geometrical imperfection in the FE model.

Material nonlinearities of the steel are incorporated through the von Mises material model with associated flow rule. The linear kinematic hardening rule, proposed by Chaboche (1985), is employed to describe the strength development of the core plate accurately under axial cyclic loading. The evolution law of this model consists of a linear kinematic hardening component that describes the translation of the yield surface in stress space through the backstress, α . This linear kinematic hardening component takes the Bauschinger effect into account, in which a reduced yield stress upon load reversal after plastic deformation has occurred during the initial loading. When temperature dependence is omitted, this evolution law is the linear Ziegler hardening law:

$$\dot{\alpha} = C \frac{1}{\sigma^0} (\sigma - \alpha) \dot{\epsilon}^{\text{pl}} \quad (26)$$

where $\dot{\epsilon}^{\text{pl}}$ is the equivalent plastic strain rate and C is the constant kinematic hardening modulus. In this model, the equivalent stress defining the size of the yield surface, σ^0 , remains constant, $\sigma^0 = \sigma_0$, where σ_0 is the equivalent stress defining the size of the yield surface at zero plastic strain. For the kinematic hardening model,

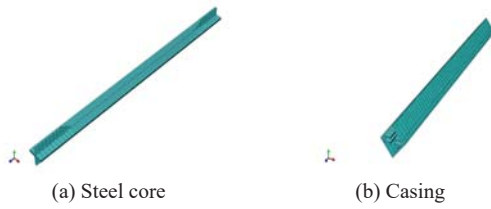


Fig. 17 Finite elements meshing of the BRB

the critical parameters including C and σ_0 are calibrated by curve fitting from the stress-strain relationship of the coupon test.

Finally, one end of the core plate is fixed and the other end is for displacement loading, only in the axial direction of core plate without any other transition or rotation. The displacement loading protocol recorded by the string potentiometer is imposed on the FE models.

5.2 Finite element results discussion

The Von-Mises stress contours of the steel BRBs at the maximum axial displacement are shown in Fig. 18. The maximum Von-Mises stress occurs on the steel core, and the region on the contact interface between the steel core and casing exhibited significant plasticity. Meanwhile, the high stress areas (red in Fig. 18(a)) are not evenly distributed along the length of the steel core, which indicates that the contact behavior occurred at the interface. Furthermore, the Von-Mises stress values for both ends of the steel core and most regions (except the contact interface) of the casing are significantly lower than the yielding strength of the steel core ($2.81 \times 10^8 \text{ N/m}^2$), which means that the connection segment and most regions of the casing are in the elastic state and possess sufficient margin to preclude the local buckling.

As listed in Tables 5, the simulation results of the Q-series specimens with respect to β are identical to the experimental results, and the strainhardening coefficients of the material are somewhat different. As for the I-1 specimen, the simulation results are slightly different from the experimental results, which might be partially attributed to the bilinear constitutive model adopted in FEM, which could not capture the behavior of ingot-iron during the fatigue tests.

Figure 19 presents the hysteretic curve comparisons of BRB specimens between the experiments and FE simulations. As shown in Fig. 19, the FE simulations of BRB specimens are in good agreement with the experimental results. Given that stiffness degradation is not well taken into account in the FE constitutive model, the simulation results are not particularly consistent with the experimental results at the unloading phase. Furthermore, the FE simulations of the specimens with ingot-iron do not particularly coincide with the experimental results at the fourth loading phase. This difference might be attributed to the fact that the

strength of the material itself is greatly enhanced after compression. In addition, the steel core of the I-1 specimen exhibits obvious multiple-wave buckling modes as shown in Fig. 11(h). In other words, the transfer of the axial force generated by the steel core to the T-shaped steel was grossly underestimated, and the Coulomb frictional model adopted in the FE simulation could not accurately capture this characteristic behavior.

Figures 20 and 21 present the equivalent secant stiffness and the equivalent viscous damping coefficient comparisons of BRB specimens between the experiments and FE simulations. As shown in Fig. 20, the FE simulations of BRB specimens show good agreement with the experimental results. The comparison results mentioned above indicate that the finite element

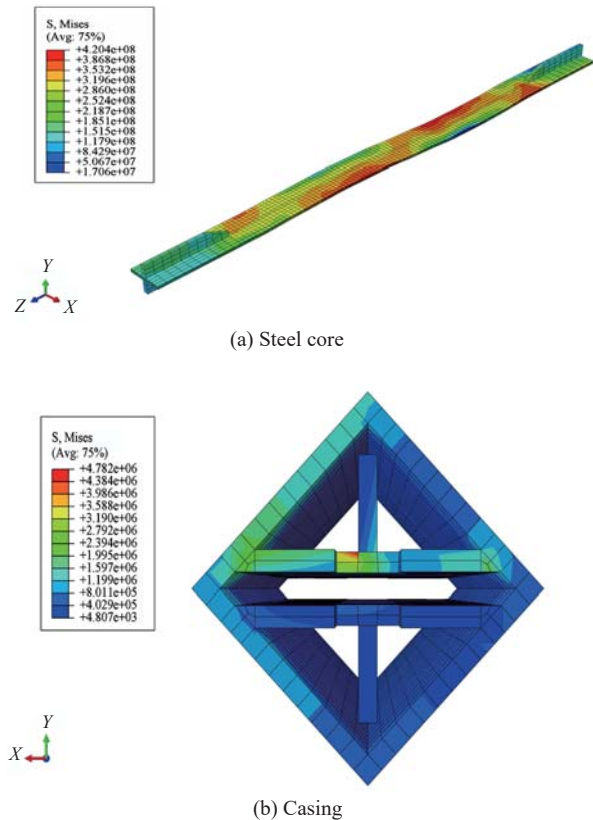


Fig. 18 Von-Mises stress contours of the BRB under maximum compression (unit: N/m^2)

Table 5 Comparisons of ω and β between experiment and simulation results

Experiment	ω	β	Simulation	ω	β
Q-1	1.26	1.07	Q-1	1.65	1.06
Q-2	1.14	1.23	Q-2	1.30	1.05
Q-3	1.35	1.12	Q-3	1.32	1.05
I-1	2.00	1.36	I-1	1.21	1.06

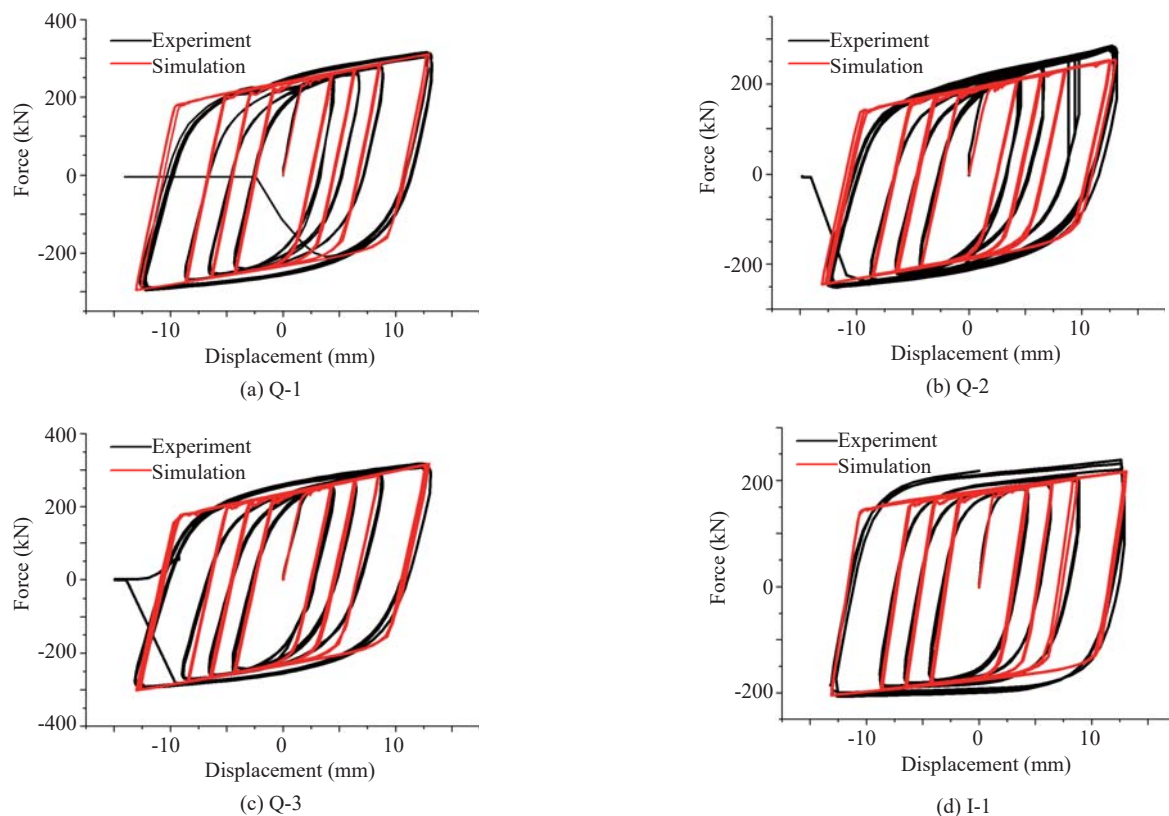


Fig. 19 Comparisons of experiment and simulation hysteretic curves of BRB specimens

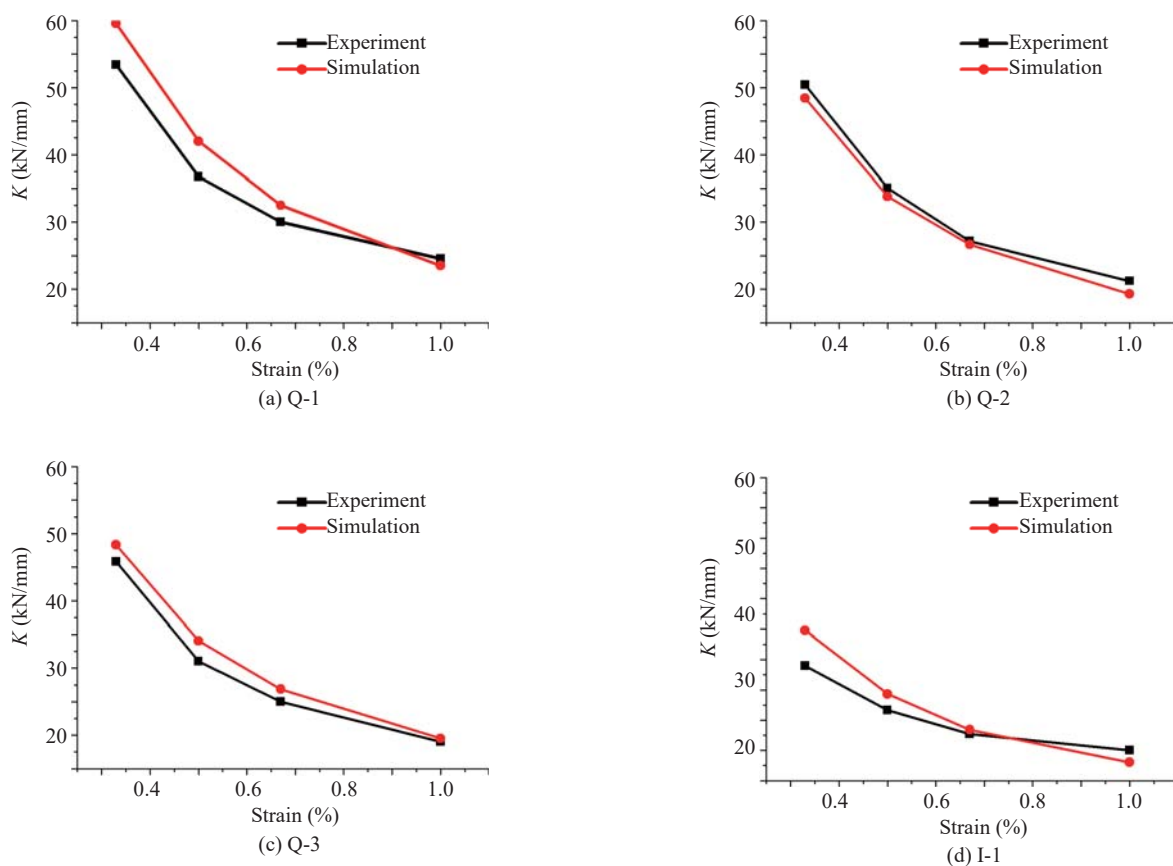


Fig. 20 Secant stiffness comparisons between experiments and simulations

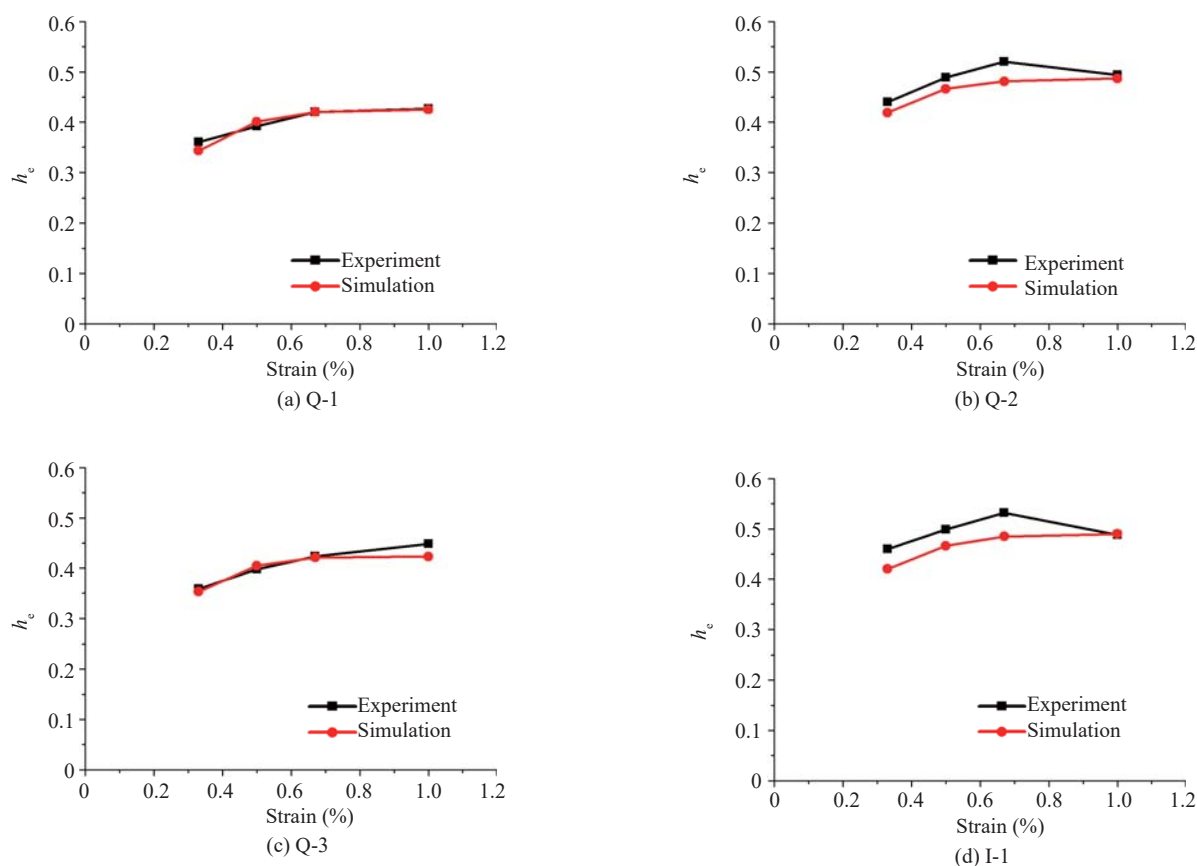


Fig. 21 Viscous damping coefficients comparisons between experiments and simulations

models adopted for simulating the performance of BRB specimens are adequate and can be utilized for further study.

6 Conclusions

In this study, a novel type of steel BRBs with the steel core made of Grade Q235-B and ingot-iron are proposed. Based on previous research, the global and local ductility demands, including local stability of the steel core and external constraint members, the gap requirements between the steel core and the casing, and the bearing capacity requirements for unrestrained nonyielding segment, etc. are discussed. In addition, quasi-static tests of eight specimens were carried out to investigate the performance of the newly proposed steel BRBs.

During the tests, no obvious bulging was observed on the casing, which validated the rationality of the design guidelines for T-shaped steel. Furthermore, all eight specimens fractured due to the tensile rupture of the steel core. Note that the Q-series specimens mainly fractured at the end of the steel core during fatigue test, while the I-series specimens mainly ruptured in the vicinity of the stopper of the core plate. In addition, the test results reveal that the seal plate welded to the external constraint elements could effectively prevent

the rupture at the end of the steel core described in Li *et al.* (2006).

The experimental results demonstrate that: 1) whatever $d = 8$ mm or 6 mm is adopted as the external angle steel, the performance of the specimens with respect to the hysteretic behavior and mechanical parameters are nearly the same, which also implies that the theory proposed in Ma (2010) is more conservative on the thickness of casing; 2) the specimens with a width-to-thickness ratio of the steel plate equal to 8 demonstrate slightly better performance, compared with the width-to-thickness ratio equal to 10 under the same conditions, which indicates that the limit of the width-to-thickness ratio of the steel core on local stability proposed in Ma (2010) seems to be premature; 3) the specimens with ingot-iron as the steel core exhibit distinguished ductility with CPD exceeding 550 and stable energy dissipation with the equivalent viscous coefficient up to 53.5%. Compared with the Q-series specimens in the same conditions, the I-series specimens also exhibit better low cycle fatigue resistance, in which all of them withstood 30 cycles of fatigue loading without premature failure. Meanwhile, as the low yielding strength steel, the compressive bearing capacity of the I-series specimens is significantly low.

Nonlinear finite element analysis has been performed to analytically investigate the behavior of all-steel BRB specimens subjected to cyclic loading. The simulation

results are basically consistent with the test results with regard to the hysteresis curves and mechanical parameters. The simulation results of the equivalent secant stiffness and the equivalent viscous damping coefficient are almost identical to the experiment results. The comparison results also reveal that the bilinear constitutive model adopted in the simulation could not accurately capture the behavior of the ingot-iron during fatigue tests, given that the strength of the material itself was greatly hardened under cyclic loading.

Acknowledgement

The authors gratefully acknowledge the financial support provided by the Basic Research Foundation of the Institute of Engineering Mechanics, CEA (2017A01), the Earthquake Scientific Research Funds Program (201508023), and the Program for Innovative Research Team in China Earthquake Administration.

References

- American Institute of Steel Construction/Structural Engineers Association of California (2001), *Recommended Provisions for Buckling-Restrained Braced Frames*. (draft)
- Black C, Makris N, and Aiken I (2002), "Component Testing, Stability Analysis and Characterization of Buckling-Restrained Braces," *Report No. Peer-2002/08*, University of California, Berkeley, CA, **2002**: 7–25.
- Black CJ, Makris N, and Aiken, ID (2004), "Component Testing, Seismic Evaluation and Characterization of Buckling-Restrained Braces," *Journal of Structural Engineering*, **130**(6): 880–894.
- Chaboche JL (1986). "Time-Independent Constitutive Theories for Cyclic Plasticity," *International Journal of Plasticity*, **2**(2): 149–188.
- Deng K, Pan P, Nie X, Xu X, Feng P and Ye L (2015), "Study of GFRP Steel Buckling Restraint Braces," *Journal of Composites for Construction*, **19**(6): (04015009)1–8.
- Dusicka P and Wiley B (2008), "Concept of Buckling Restraint of Steel Braces with Fiber Reinforced Polymers," *Structures Congress 2008: Crossing Borders*, 1–7.
- Eryaşar ME and Topkaya C (2010), "An Experimental Study on Steel-Encased Buckling-Restrained Brace Hysteretic Dampers," *Earthquake Engineering & Structural Dynamics*, **39**(5): 561–581.
- Fahnestock LA, Sause R, Ricles JM and Lu LW (2003), "Ductility Demands on Buckling-Restrained Braced Frames under Earthquake Loading," *Earthquake Engineering and Engineering Vibration*, **2**(2): 255–268.
- Fukuda K, Makino T and Ichinohe Y (2004), "Development of Brace-Type Hysteretic Dampers," *Summaries of Technical Papers of Annual Meeting*, Vol. 8, Architectural Institute of Japan, 867–868.
- GB 50017-2017 (2017), *Industry standard of the People's Republic of China, T Chinese technical specification for steel structure*, Ministry of Housing and Urban-Rural Development of the People's Republic of China, Beijing: China Architecture & Building Press (in Chinese)
- Hoveidae N, and Rafezy B (2015), "Local Buckling Behavior of Core Plate in All-Steel Buckling Restrained Braces," *International Journal of Steel Structures*, **15**(2): 249–260.
- JGJ 99-2015 (2015), *Industry Standard of the People's Republic of China, Technical Specification for Steel Structure of Tall Buildings*, Ministry of Housing and Urban-Rural Development of the People's Republic of China, Beijing: China Architecture & Building Press. (in Chinese)
- Jiang ZQ (2014), *Theoretical and Experimental Study on Design Methods for Double Square Tube Assembled Buckling-Restrained Brace*, Beijing: Tsinghua University. (in Chinese)
- Kimura K, Yoshioka K and Takeda T (1976), "Tests on Braces Encased by Mortar In-Filled Steel Tubes," *Summaries of Technical Papers of Annual Meeting*, Architectural Institute of Japan, **1041**: 1–42.
- Koetaka Y, Tsujita O and Narihara H (2000), "The Experimental Study on Buckling Restrained Braces (Part 2 Experiment on Rigid Connection Type)," *Summaries of Technical Papers of Annual Meeting*, Architectural Institute of Japan, **9**: 913–914.
- Kuwahara S, Tada M, Yoneyama T and Imai K (1993), "A Study on Stiffening Capacity of Double-Tube Members," *Journal of Structural and Construction Engineering*, **445**(3): 151–158.
- Li Wei, Wu Bin, and Ding Yong (2013), "Experimental Study on Seismic Behaviors of H-Section Steel Buckling-Restrained Braces," *Journal of Building Structures*, **34**(12): 94–102. (in Chinese)
- Li Yan, Wu Bin, Wu QY and Ou JP (2006), "An Experimental Study of Anti-Buckling Steel Damping-Braces," *China Civil Engineering Journal*, **39**(7): 9–14. (in Chinese)
- López-Almansa F, Castro-Medina JC and Oller S (2012), "A Numerical Model of the Structural Behavior of Buckling-Restrained Braces," *Engineering Structures*, **41**: 108–117.
- Ma Ning, Wu Bin and Zhao JX (2010), "Full Scale Uniaxial and Subassemblage Tests on the Seismic Behavior of All-Steel Buckling-Resistant Brace," *China Civil Engineering Journal*, **43**(4): 1–7. (in Chinese)
- Ma Ning (2010), "Seismic Behavior and Design Method of All-Steel Buckling Restrained Braces and Steel Frames," *PhD Thesis*, Harbin Institute of Technology. (in Chinese)
- Miller DJ, Fahnestock LA and Eatherton MR (2012),

“Development and Experimental Validation of a Nickel–Titanium Shape Memory Alloy Self-Centering Buckling-Restrained Brace,” *Engineering Structures*, **40**: 288–298.

Mochizuki S and Murata Y (1979), “Experimental Study on Buckling of Unbonded Braces Under Axial Forces,” *Summaries of Technical Papers of Annual Meeting*, Architectural Institute of Japan, 1623–1626.

Newell, J, Uang CM and Benzoni G (2006), “Sub-Assemblage Testing of Corebrace Buckling-Restrained Braces (G series),” *Report No. TR-06/-1*, University of California, San Diego.

Sasaki J, Nagao T and Sakaguchi T (2008), “Studies on Buckling-Restrained Bracing Using Triple Steel Tubes: Part 7: Consideration on Experimental Results of Full Scale Tests,” *Summaries of Technical Papers of Meeting*, Architectural Institute of Japan, 31–42.

Takeita K, Nagao T and Taguti T (2005), “Studies on Buckling-Restrained Brace Using Triple Steel Tubes Part 2: Consideration on Experimental Results and Finite Element Method Analysis,” *Summaries of Technical Papers of Annual Meeting*, C-1, Tokyo: Architectural

Institute of Japan, 1013–1014.

Tsai CS, Lin Y, Chen W and Su HC (2009), “Mathematical Modeling and Full-Scale Shaking Table Tests for Multi-Curve Buckling Restrained Braces,” *Earthquake Engineering & Engineering Vibration*, **8**(3): 359–371.

Wakabayashi M, Nakamura T and Kashibara A (1973), “Experimental Study of Elastoplastic Properties of Precast Concrete Wall Panels with Built-In Insulating Braces,” *Summaries of Technical Papers of Annual Meeting*, Vol. 104121044, Architectural Institute of Japan, 12–20.

Watanabe A, Hitomi Y, Saeki E, Wada A and Fujimoto M (1988), “Properties of Brace Encased in Buckling-Restraining Concrete and Steel Tube,” *Proceedings of Ninth World Conference on Earthquake Engineering*, **4**: 719–724.

Wang HQ, Ding JM and He ZJ (2007), “The Application and Design of Buckling-Restrained Braces,” *Structure Engineers*, **23**(4): 6–11. (in Chinese)

Wu Yong (2008), “Finite Element Analysis of Seismic Behavior of All-Steel Buckling-Restrained Braces,” Harbin Institute of Technology. (in Chinese)